Breathing and switching cyclops states in Kuramoto networks with higher-mode coupling

Maxim I. Bolotov,[1] Vyacheslav O. Munyayev,[1] Lev A. Smirnov,[1] Grigory V. Osipov,[1] and Igor Belykh[2,*]
[1]*Department of Control Theory, Lobachevsky State University of Nizhny Novgorod, 23 Gagarin Avenue, Nizhny Novgorod, 603022, Russia*
[2]*Department of Mathematics and Statistics and Neuroscience Institute, Georgia State University, P.O. Box 4110, Atlanta, Georgia 30302-410, USA*

(Received 8 January 2024; accepted 10 April 2024; published 6 May 2024)

Cyclops states are intriguing cluster patterns observed in oscillator networks, including neuronal ensembles. The concept of cyclops states formed by two distinct, coherent clusters and a solitary oscillator was introduced by Munyaev *et al.* [Phys. Rev. Lett. **130**, 107201 (2023)], where we explored the surprising prevalence of such states in repulsive Kuramoto networks of rotators with higher-mode harmonics in the coupling. This paper extends our analysis to understand the mechanisms responsible for destroying the cyclops' states and inducing dynamical patterns called breathing and switching cyclops states. We first analytically study the existence and stability of cyclops states in the Kuramoto-Sakaguchi networks of two-dimensional oscillators with inertia as a function of the second coupling harmonic. We then describe two bifurcation scenarios that give birth to breathing and switching cyclops states. We demonstrate that these states and their hybrids are prevalent across a wide coupling range and are robust against a relatively large intrinsic frequency detuning. Beyond the Kuramoto networks, breathing and switching cyclops states promise to strongly manifest in other physical and biological networks, including coupled theta neurons.

DOI: 10.1103/PhysRevE.109.054202

I. INTRODUCTION

Phase oscillator networks have emerged as a paradigmatic reduced model for describing emergent cooperative properties of diverse real-world systems, including neuronal networks [1–3], laser arrays [4–6], and power grids [7–9]. The celebrated Kuramoto model of one-dimensional (1D) oscillators [10,11] and its extension to two-dimensional (2D) oscillators with inertia [12] captures the essence of the phase networks and provides a concise framework to explore the richness of their cooperative dynamics [13–19]. These dynamics include full [20–24], partial [25,26], explosive [27–29] and asymmetry-induced synchronization [30,31], chimeras [32–39], solitary states [40–44], clusters [45–48], generalized splay [49], and cyclops states [50]. The cooperative dynamics of Kuramoto networks with attractive coupling have been studied more extensively than their counterparts in repulsive networks. While full synchronization is the simplest and most dominant rhythm in attractive networks, splay [51,52] and generalized and cluster splay states [48,49] are expected to be the most probable patterns in repulsive networks. Yet a complete understanding of rhythmogenesis in repulsive networks is still lacking. Two repulsively coupled oscillators tend to achieve antiphase synchronization; however, predicting an outcome of such interactions in large repulsive networks is often elusive. Notably, the role of repulsive connections can be counterintuitive, especially in networks with mixed attractive and repulsive coupling [53–56]. For example, adding pairwise repulsive inhibition to excitatory networks of bursting neurons can synergistically promote synchronization by facilitating transitions between different types of bursting [55].

In the context of Kuramoto-type networks, the prevailing approach is to model interactions by the first sinusoidal harmonic from a Fourier decomposition of a 2π-periodic coupling function. This simplest choice of the coupling form adequately describes many dynamical features of real-world networks and is analytically tractable. However, higher-order coupling harmonics have been observed to play a significant role in rhythmogenesis in various scenarios. These encompass Kuramoto-type models of neuronal plasticity [57,58], coupled electrochemical oscillators [59], and Josephson junctions [60]. In particular, previous research has demonstrated that augmenting the classical Kuramoto model with higher-mode coupling can result in the emergence of multiple phase-locked states [61,62] and facilitate switching between synchrony clusters [63].

In a recent work [50], we studied rhythmogenesis in repulsive Kuramoto networks of identical 2D phase oscillators with phase-lagged first-mode and higher-mode coupling. We introduced the concept of cyclops states formed by two distinct, coherent clusters and a solitary oscillator reminiscent of the Cyclops's eye. These cyclops states represent a particular class of three-cluster generalized splay states [49] with the solitary oscillator maintaining constant phase differences with the coherent clusters. We reported a surprising finding that adding the second or third harmonic to the Kuramoto coupling makes the cyclops state global attractors in a wide range of couplings' repulsion. Beyond Kuramoto networks, we showed that the stabilization of cyclops states by the higher coupling harmonics is also robustly present in theta neurons with adaptive coupling.

*Corresponding author: ibelykh@gsu.edu

This paper extends our previous analysis to reveal higher-mode coupling-induced mechanisms for emerging dynamical patterns termed breathing and switching cyclops states. Toward this goal, we derive analytical conditions on the existence and stability of cyclops states with constant intercluster phases in the presence of the second coupling harmonic. These conditions reveal two bifurcation scenarios for destabilizing the cyclops states. In the first scenario, the cyclops states with constant intercluster phases between its three clusters undergo an Andronov-Hopf bifurcation, preserving their intracluster formations but making the intercluster relative phase differences oscillate periodically. Similarly to breathing three-cluster patterns introduced in [47], we call these breathing cyclops states. These states can evolve into rotobreathers with intercluster phase differences governed by mixed-mode, oscillatory-rotatory phase difference dynamics. In the second bifurcation scenario, the cyclops state with constant intercluster phases loses its structural stability but quickly reforms into a new cyclops state with a reshuffled configuration. This repetitive switching process yields switching cyclops states. These states are similar to blinking chimeras, also characterized by a death-birth process in which the coherent cluster dissolves and is quickly reborn in a new configuration [64].

We show that breathing, rotobreathing, and switching cyclops states are stable in a wide range of the second harmonic coupling strength and phase lag parameter. Remarkably, breathing and rotobreathing cyclops states are dominant states, acting as the system's global attractors in a large interval of the second harmonic's phase lag parameter, corresponding to the overall repulsiveness of the combined first- and second-harmonic coupling. We also demonstrate that the cyclops states can robustly emerge in Kuramoto networks of nonidentical oscillators. In [50], we proved that the 2D Kuramoto model with the first and second-harmonic coupling is dynamically equivalent to a network of canonical theta neurons with adaptive coupling. Therefore, we expect breathing and switching cyclops states to manifest strongly in theta-neuron networks, pointing to the broader applicability of our results.

The layout of this paper is as follows. In Sec. II we introduce the oscillator network model and state the problem under consideration, and give formal definitions. In Sec. III we study the existence of cyclops states with constant intercluster phase differences, called stationary cyclops states. We derive an upper bound for the maximum number of stationary cyclops states with distinct intercluster phase differences. In Sec. IV we derive a four-dimensional (4D) system that governs the dynamics of the intercluster phase differences. We study the stability of the fixed point of the 4D system, which corresponds to constant intercluster phase differences. We derive the conditions under which the fixed point undergoes an Andronov-Hopf bifurcation, giving rise to a breathing cyclops state. In Sec. V we analyze the variational equations for the transversal stability of stationary cyclops states that determines the stability of their coherent clusters. In Sec. VI we numerically study breathing and switching cyclops states emerging from stationary cyclops states via two distinct bifurcation routes. We demonstrate the emergence of more complex, hybrid dynamical patterns that combine the properties of both breathing and switching cyclops states. We also study the prevalence of different cyclops states and show that they robustly appear from large sets of randomly chosen initial conditions. In Sec. VII we show the persistence of cyclops states against relatively large intrinsic frequency detuning. Section VIII contains concluding remarks and discussions. The Appendix contains the derivation of the upper bound for the maximum number of stationary cyclops states.

II. THE MODEL AND PROBLEM STATEMENT

We consider the Kuramoto-Sakaguchi network of 2D phase oscillators

$$\mu\ddot{\Theta}_k + \dot{\Theta}_k = \omega + \sum_{n=1}^{N}\sum_{q=1}^{2}\frac{\varepsilon_q}{N}\sin[q(\Theta_n - \Theta_k) - \alpha_q], \quad (1)$$

where the kth oscillator's phase Θ_k ranges from $-\pi$ to π, and the second-order Kuramoto-Sakaguchi coupling [65] represents a pairwise interaction function $H(\Theta_n - \Theta_k) = \sum_{q=1}^{2}\varepsilon_q \sin[q(\Theta_n - \Theta_k) - \alpha_q]$. The oscillators are assumed to be identical with frequency ω, inertia μ, and phase lag parameters α_1 and α_2. We consider the phase lag $\alpha_1 \in (\pi/2, \pi)$, that makes the first-harmonic coupling repulsive and fix $\varepsilon_1 = 1$ that corresponds to a strong first-harmonic coupling. Throughout the paper, we also choose and fix a relatively strong inertia $\mu = 1$ that is sufficient to make the dynamics of the 2D system qualitatively distinct from the 1D classical model and enable the emergence of breathing cluster dynamics [46]. We will consider a broader range of $\alpha_2 \in (-\pi, \pi)$, so that the second harmonic may be pairwise attractive or repulsive. As a result, the overall combined coupling may be repulsive with $H'(0) < 0$ or attractive with $H'(0) > 0$. The latter is possible when the second-harmonic coupling ε_2 is sufficiently strong to overcome the first-harmonic coupling contribution.

Phase coherence and cluster synchrony in the system (1) can be characterized via the lth-order complex Kuramoto parameters [63,66]:

$$R_l(t) = \frac{1}{N}\sum_{k=1}^{N} e^{il\Theta_k} = r_l e^{i\psi_l},$$

where r_l and ψ_l define the magnitude and the phase of the lth moment Kuramoto order parameter $R_l(t)$, respectively. The first-order scalar parameter $r_1 = |R_1|$ characterizes the degree of phase synchrony with $r_1 = 1$ corresponding to full phase synchrony. Splay states or generalized splay states $\Theta_k = \omega t + \varphi_k$, $k = 1, \ldots, N$ with constant nonuniform relative phases $\varphi_k \in [-\pi, \pi]$ satisfy the condition $r_1 = 0$ in the 2D Kuramoto model with the first-harmonic coupling ($\varepsilon_2 = 0$). The second-order scalar parameter $r_2 = |R_2|$ determines the degree of cluster synchrony. In the case of the first-harmonic coupling ($\varepsilon_2 = 0$), r_2 controls the stability of generalized splay states so that increasing r_2 enlarges their stability parameter regions [49,50]. It was shown in [50] that generalized splay states with a maximum r_2 are (i) two-cluster symmetric splay states (for even N) and (ii) three-cluster splay states with the relative phases (for odd N):

$$\varphi_1 = \varphi_2 = \cdots = \varphi_{M-1} = \gamma, \quad \varphi_M = 0,$$
$$\varphi_{M+1} = \cdots = \varphi_N = -\gamma, \quad (2)$$

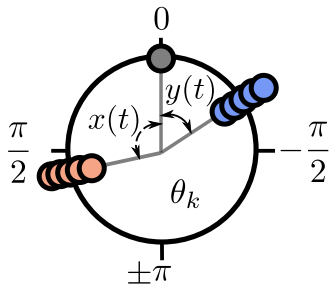

FIG. 1. Snapshot of a breathing cyclops state in network (1) of 11 oscillators. Periodically oscillating $x(t)$ and $y(t)$ govern the phase difference between the synchronous clusters (blue and pink circles) and the solitary oscillator (gray circle). The solitary oscillator's phase is chosen at $\theta_M = 0$ as a reference. Parameters are $\alpha_1 = 1.7$, $\varepsilon_2 = 0.08$, $\alpha_2 = -0.3$.

where $\gamma = \arccos[1/(1-N)]$, $M = (N+1)/2$, and the choice of the reference zero phase for φ_M is arbitrary. We termed three-cluster splay states (2) cyclops states. Adding the second-harmonic coupling with $\varepsilon_2 \neq 0$ breaks their symmetry in γ and makes r_1 nonzero, albeit small. We demonstrated in [50] that the second- or higher-harmonic coupling can make these asymmetric patterns dominant states. In this paper, we generalize the definition of cyclops states (2) for the system (1) with second-harmonic coupling and odd N by relaxing the condition $r_1 = 0$. As a result, we refer to the following three-cluster state determined by the three-dimensional cluster manifold:

$$D(3) = \begin{cases} \Theta_1(t) = \cdots = \Theta_{M-1}(t) = x + \Omega t, \\ \Theta_M(t) = \Omega t, \\ \Theta_{M+1}(t) = \cdots = \Theta_N(t) = y + \Omega t \end{cases} \tag{3}$$

as to a *stationary cyclops state* in which two equal clusters of $M-1$ oscillators rotate with the common frequency Ω, preserving the stationary phase differences $x = \gamma_1$, and $y = \gamma_2$ with the Mth solitary oscillator. Note that due to the asymmetry of the relative phases $x \neq y$, the common rotational frequency Ω differs from the oscillators' intrinsic frequency ω and can be derived explicitly from (1) as shown in the next section.

Similarly to (2), the stationary cyclops state defined by (3) can be conveniently represented within the reference frame $\theta_k = \Theta_k - \Omega t$, $k = 1, \ldots, N$ where the relative constant phase of the Mth oscillator, θ_M, is chosen at zero so that

$$\begin{aligned} \theta_1 = \cdots = \theta_{M-1} = x, \quad \theta_M = 0, \\ \theta_{M+1} = \cdots = \theta_N = y. \end{aligned} \tag{4}$$

Due to the system's global coupling symmetry and equal cluster sizes $M-1$, the existence of the stationary cyclops state with intercluster phase differences $x = \gamma_1$ and $y = \gamma_2$ implies the existence of its counterpart with $x = \gamma_2$ and $y = \gamma_1$. Thus, cyclops states exist in symmetrical pairs. In the following, we will analyze the existence and stability of stationary cyclops states in the system (1) with odd N. We will describe two main scenarios for destabilizing a stationary cyclops state that yield (i) *a breathing cyclops state* with periodically oscillating $x(t)$, $y(t)$ so that the intercluster phase differences are bounded as $|x(t)| < \pi$, $|y(t)| < \pi$ to produce no phase slips (Fig. 1) and (ii) *a switching cyclops state*, representing a repetitive death-birth process in which the clusters disintegrate to form a new cyclops state with a new reshuffled cluster configuration and a new solitary node.

We will also study how the breathing and switching cyclops states can (i) further evolve into more complex dynamical patterns, including hybrid switching-breathing states, (ii) become globally stable, and (iii) persist against intrinsic frequency detuning.

III. POSSIBLE CONSTANT INTERCLUSTER PHASE DIFFERENCES

We seek to find permissible stationary cyclops states as a function of the system's parameters. To determine the constant phase differences x, y, and the rotational frequency Ω, we substitute the stationary cyclops state solution (3) into (1) and obtain the system of nonlinear transcendental equations:

$$\begin{aligned} &\omega - \Omega - \sum_{q=1}^{2} \frac{\varepsilon_q}{N} \Bigg(\sin(qx + \alpha_q) + \frac{N-1}{2} \{ \sin \alpha_q \\ &\quad + \sin[q(x-y) + \alpha_q] \} \Bigg) = 0, \\ &\omega - \Omega - \sum_{q=1}^{2} \frac{\varepsilon_q}{N} \Bigg(\sin \alpha_q - \frac{N-1}{2} [\sin(qx - \alpha_q) \\ &\quad + \sin(qy - \alpha_q)] \Bigg) = 0, \\ &\omega - \Omega - \sum_{q=1}^{2} \frac{\varepsilon_q}{N} \Bigg(\sin(qy + \alpha_q) + \frac{N-1}{2} \{ \sin \alpha_q \\ &\quad + \sin[q(y-x) + \alpha_q] \} \Bigg) = 0. \end{aligned} \tag{5}$$

We subtract the second equation from the first and third equations of (5) to eliminate Ω and obtain the system of two equations for finding the unknown constants x and y:

$$\begin{aligned} &\frac{N-3}{2} \sum_{q=1}^{2} \varepsilon_q \sin \alpha_q + \sum_{q=1}^{2} \varepsilon_q \sin(qx + \alpha_q) \\ &\quad + \frac{N-1}{2} \Bigg(\sum_{q=1}^{2} \varepsilon_q \sin(qx - \alpha_q) + \sum_{q=1}^{2} \varepsilon_q \sin(qy - \alpha_q) \\ &\quad - \sum_{q=1}^{2} \varepsilon_q \sin[q(y-x) - \alpha_q] \Bigg) = 0, \\ &\frac{N-3}{2} \sum_{q=1}^{2} \varepsilon_q \sin \alpha_q + \sum_{q=1}^{2} \varepsilon_q \sin(qy + \alpha_q) \\ &\quad + \frac{N-1}{2} \Bigg(\sum_{q=1}^{2} \varepsilon_q \sin(qx - \alpha_q) + \sum_{q=1}^{2} \varepsilon_q \sin(qy - \alpha_q) \\ &\quad - \sum_{q=1}^{2} \varepsilon_q \sin[q(x-y) - \alpha_q] \Bigg) = 0. \end{aligned} \tag{6}$$

In turn, we find the rotational frequency Ω from the second equation of (5):

$$\Omega = \omega - \frac{1}{N}\sum_{q=1}^{2}\varepsilon_q \sin\alpha_q + \frac{N-1}{2N}\left[\sum_{q=1}^{2}\varepsilon_q \sin(qx-\alpha_q)+\sum_{q=1}^{2}\varepsilon_q \sin(qy-\alpha_q)\right] \tag{7}$$

with x and y calculated from (6).

Due to the complexity of system (6), its solution for x and y cannot be found in closed form. Yet we derive an upper bound for the maximum number of stationary cyclops states with distinct x and y. To do so, we transform the real-valued system (6) into a system of complex polynomial equations and apply the Bernshtein theorem [67], a practical tool in algebra that bounds the number of nonzero complex solutions by the mixed volume of their Newton polytopes. The details of this analysis are quite technical and are delegated to the Appendix. This analysis shows that the complex form of system (6) may have up to 17 possible solutions (including some nonphysical) corresponding up to 16 stationary cyclops states with distinct ordered pairs of constant phase differences x, y. As stationary cyclops states exist in pairs, there may be at most eight combinations of x, y (up to the cluster permutation $x \longleftrightarrow y$). It is worth noticing that there is a continuum of stationary cyclops states with a given pair (x, y) due to an arbitrary choice of the reference solitary state's phase θ_M.

Figure 2 displays the number of different stationary cyclops states calculated by solving the complex polynomial equation (A1) using the NSolve function of Wolfram *Mathematica*. Note that this number equals two for small values of the second-harmonic amplitude ε_2. This pair of stationary cyclops states with $x = \gamma_1$ and $y = \gamma_2$ ($x = \gamma_2$ and $y = \gamma_1$) emerges continuously from the symmetrical cyclops state (2) that exists in the system (1) in the absence of the second-harmonic coupling ($\varepsilon_2 = 0$). As Figs. 2(a) and 2(b) indicate, increasing ε_2 increases the number of coexisting stationary cyclops states and induces richer dynamics. In the following, we will derive general stability conditions for a permissible stationary cyclops state and specify these conditions to the cyclops state (4) with $x = \gamma_1$ and $y = \gamma_2$ from the dashed parameter region in Fig. 2 where no other cyclops states with distinct x and y (up to permutation of clusters $x \longleftrightarrow y$) exist.

IV. STABILITY OF THE INTERCLUSTER PHASE DIFFERENCES

We seek to obtain the conditions for the stability of the constant intercluster phase differences to small perturbations of x and y. The dynamics of the intercluster phase differences are governed by the system

$$\mu\ddot{x}+\dot{x} = \sum_{q=1}^{2}\frac{\varepsilon_q}{N}(\sin\alpha_q - \sin(qx+\alpha_q) - \frac{N-1}{2}[\sin(qx-\alpha_q)+\sin(qy-\alpha_q) + \sin\alpha_q + \sin[q(x-y)+\alpha_q]]),$$

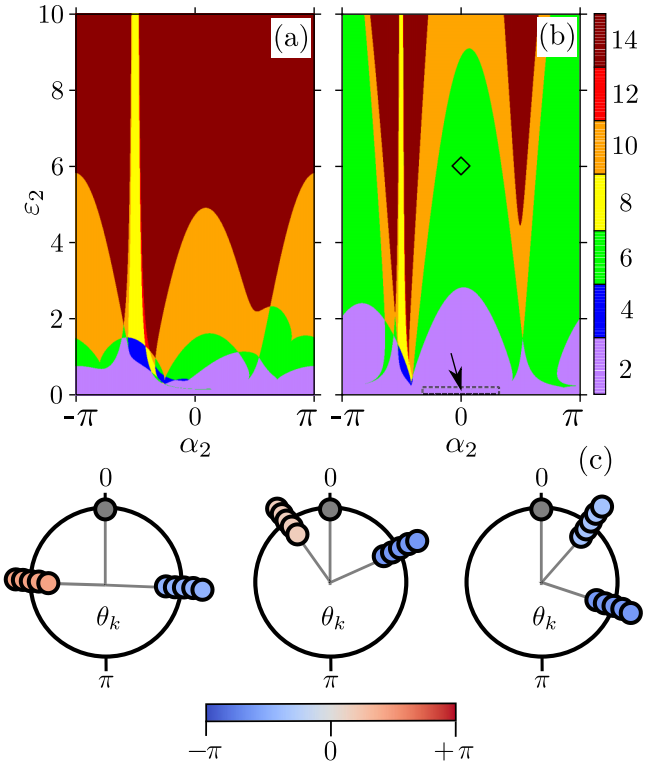

FIG. 2. (a, b) The color shows the number of distinct stationary cyclops states in the network (1) as a function of the second-harmonic coupling and phase lag parameters $(\alpha_2, \varepsilon_2)$. Other parameters are (a) $N = 5$, $\alpha_1 = 2.0$ and (b) $N = 11$, $\alpha_1 = 1.7$. The number of cyclops is calculated by numerically finding solutions of system (6). The arrow points to the dashed area corresponding to the stability diagram of Fig. 3. (c) Snapshots of three distinct stationary cyclops states (up to permutation of clusters $x \longleftrightarrow y$) for the parameter set $N = 11$, $\alpha_1 = 1.7$, $\alpha_2 = 0.0$, $\varepsilon_2 = 6.0$ corresponding to the open diamond in the green area in panel (b). The oscillator coloring corresponds to the intercluster differences x and y according to positive and negative values depicted from the horizontal color bar.

$$\mu\ddot{y}+\dot{y} = \sum_{q=1}^{2}\frac{\varepsilon_q}{N}(\sin\alpha_q - \sin(qy+\alpha_q) - \frac{N-1}{2}\{\sin(qx-\alpha_q)+\sin(qy-\alpha_q) + \sin\alpha_q + \sin[q(y-x)+\alpha_q]\}). \tag{8}$$

The 4D dynamical system (8) may be viewed loosely as a system of two nonlinearly coupled driven pendulum-like equations with the terms $\sin\alpha_q$ representing constant torques and the sine terms with x and y corresponding to pendulum-like nonlinearities and coupling. The presence of the second-harmonic coupling prevents transforming the system (8) into a more explicit system of two coupled pendula as was achieved for a three-cluster state in [47]. However, the pendulum-like structure of the 4D system (8) points to the possible existence of nontrivial dynamics related to oscillating and even chaotically evolving intercluster phase differences $x(t)$ and $y(t)$.

Fixed points of system (8) correspond to constant intercluster phase differences x, y calculated from (6). We aim to study

the local stability of the fixed points and derive bifurcation conditions that induce oscillating phase differences $x(t)$, $y(t)$. Toward this goal, we consider small deviations $\delta x(t)$ and $\delta y(t)$ from a fixed point $x = \gamma_1$, $y = \gamma_2$ corresponding to a stationary cyclops state. So $x(t) = \gamma_1 + \delta x(t)$, $y(t) = \gamma_2 + \delta y(t)$. We linearize the system (8) in the vicinity of the fixed point state and obtain the following equations that govern the evolution of small deviations $\delta x(t)$ and $\delta y(t)$:

$$\mu\delta\ddot{x} + \delta\dot{x} = -\sum_{q=1}^{2}\frac{\varepsilon_q q}{N}\left[\cos(q\gamma_1+\alpha_q)\delta x + \frac{N-1}{2}[\cos(q\gamma_1-\alpha_q)\delta x + \cos(q\gamma_2-\alpha_q)\delta y + \cos(q\sigma+\alpha_q)(\delta x-\delta y)]\right],$$
$$\mu\delta\ddot{y} + \delta\dot{y} = -\sum_{q=1}^{2}\frac{\varepsilon_q q}{N}\left[\cos(q\gamma_2+\alpha_q)\delta y + \frac{N-1}{2}[\cos(q\gamma_1-\alpha_q)\delta x + \cos(q\gamma_2-\alpha_q)\delta y + \cos(q\sigma-\alpha_q)(\delta y-\delta x)]\right], \tag{9}$$

where $\sigma = \gamma_1 - \gamma_2$.

Following the standard stability approach, we seek solutions $\delta x(t) = A_1 e^{\lambda t}$, $\delta y(t) = A_2 e^{\lambda t}$ and derive a system of two characteristic equations for finding constants λ, A_1, and A_2:

$$(\mu\lambda^2+\lambda)A_1 = -(p_{11}A_1 + p_{12}A_2),$$
$$(\mu\lambda^2+\lambda)A_2 = -(p_{21}A_1 + p_{22}A_2), \tag{10}$$

where

$$p_{11} = \sum_{q=1}^{2}\frac{\varepsilon_q q}{N}\left\{\frac{N-1}{2}[\cos(q\gamma_1-\alpha_q)+\cos(q\sigma+\alpha_q)] + \cos(q\gamma_1+\alpha_q)\right\},$$
$$p_{12} = \sum_{q=1}^{2}\frac{\varepsilon_q q}{N}\left\{\frac{N-1}{2}[\cos(q\gamma_2-\alpha_q)-\cos(q\sigma+\alpha_q)]\right\},$$
$$p_{21} = \sum_{q=1}^{2}\frac{\varepsilon_q q}{N}\left\{\frac{N-1}{2}[\cos(q\gamma_1-\alpha_q)-\cos(q\sigma-\alpha_q)]\right\},$$
$$p_{22} = \sum_{q=1}^{2}\frac{\varepsilon_q q}{N}\left\{\frac{N-1}{2}[\cos(q\gamma_2-\alpha_q)+\cos(q\sigma-\alpha_q)] + \cos(q\gamma_2+\alpha_q)\right\}. \tag{11}$$

Solving the characteristic system (10) of two coupled quadratic equations to explicitly find λ is out of reach. Instead, we introduce the variable $\Lambda = \mu\lambda^2 + \lambda$ and turn the system (10) into the system of linear equations

$$\boldsymbol{P}(A_1, A_2)^T = \Lambda(A_1, A_2)^T, \tag{12}$$

where

$$\boldsymbol{P} = \begin{pmatrix} -p_{11} & -p_{12} \\ -p_{21} & -p_{22} \end{pmatrix}. \tag{13}$$

Therefore, the stability of (9) can be assessed from (13) in terms of its eigenvalues Λ. To do so, we aim to determine the boundary of the stability region that is determined by $\lambda = i\,\mathrm{Im}\lambda$ and corresponds to an Andronov-Hopf bifurcation of the fixed point that induces oscillating phase differences $x(t)$ and $y(t)$. Therefore, we can set $\mathrm{Re}\Lambda + i\,\mathrm{Im}\Lambda = -\mu(\mathrm{Im}\lambda)^2 + i\,\mathrm{Im}\lambda$ so that the real part equality $\mathrm{Re}\Lambda + \mu(\mathrm{Im}\Lambda)^2 = 0$ defines the stability boundary $\lambda = i\mathrm{Im}\lambda$. To ascertain what side of the stability boundary corresponds to stability, we select the test value $\mu = 0$. With this choice, we have $\Lambda = \lambda$, and the inequality $\mathrm{Re}\Lambda < 0$ ensures the stability of the fixed point. Extending this argument to nonzero μ, we can conclude that the inequality $\mathrm{Re}\Lambda + \mu(\mathrm{Im}\Lambda)^2 < 0$ makes $\mathrm{Re}\lambda < 0$ and determines the fixed point stability. Thus, we arrive at the following assertion.

Statement 1. [Internal stability of stationary cyclops states].

1. Constant intercluster phase differences $x = \gamma_1$ and $y = \gamma_2$ of the stationary cyclops state (3) are locally stable iff

$$\mathrm{Re}\Lambda_{1,2} + \mu(\mathrm{Im}\Lambda_{1,2})^2 < 0,$$
$$\Lambda_{1,2} = \frac{\mathrm{Tr}\boldsymbol{P}}{2} \pm \frac{\sqrt{(\mathrm{Tr}\boldsymbol{P})^2 - 4\det\boldsymbol{P}}}{2}, \tag{14}$$

where $\mathrm{Tr}\boldsymbol{P}$ and $\det\boldsymbol{P}$ are, respectively, the trace and determinant of matrix $\boldsymbol{P}$ (13) whose coefficients are defined in (11).

2. The stability boundary

$$\mathrm{Re}\Lambda_{1,2} + \mu(\mathrm{Im}\Lambda_{1,2})^2 = 0 \tag{15}$$

corresponds to an Andronov-Hopf bifurcation that destabilizes the stationary cyclops state, turning it into a breathing cyclops state with oscillating intercluster phase differences $x(t)$ and $y(t)$.

The stability of constant phase differences x and y defined via (14) can be interpreted as the internal (longitudinal) stability of the stationary cyclops state within the invariant three-cluster manifold D determined by (3) with arbitrary, possibly time-varying $x(t)$ and $y(t)$. The stability boundary (15) depicted by the blue solid curve in Fig. 3(a) corresponds to emerging instability of constant phase differences x and y that preserves the three-cluster cyclops formation on the invariant three-cluster manifold D.

Having studied the stability of the constant intercluster phase differences, we proceed with the stability analysis of the synchronous clusters, each composed of $M-1$ oscillators. These conditions, paired with the condition (14), shall indicate what stationary cyclops states can stably emerge in the network.

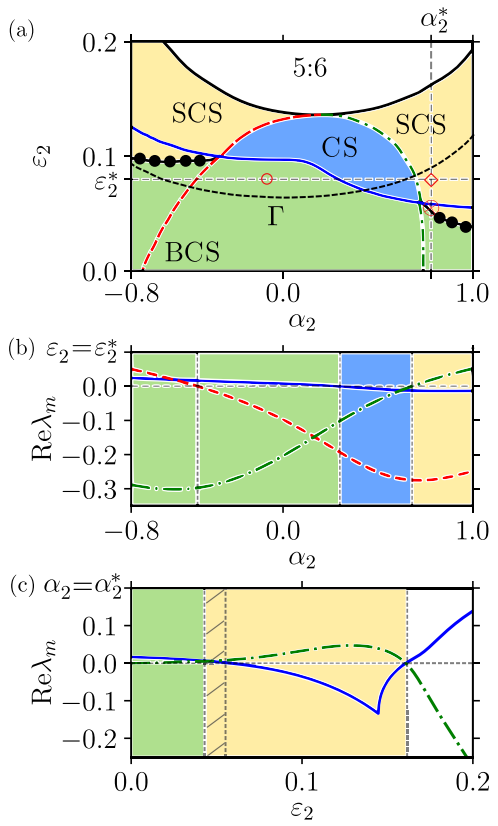

FIG. 3. (a) The stability diagram for cyclops states. Regions of stable stationary cyclops states (CS) are shown in blue, switching cyclops states (SCS) in yellow, breathing cyclops states (BCS) in green, and two-cluster regimes (5:6) in white. Analytical boundaries: the blue solid line corresponds to the stability boundary (15), the red dashed line to $\mathrm{Re}\lambda_1^{\mathrm{tran}} = 0$, and the green dash-dotted curve to $\mathrm{Re}\lambda_2^{\mathrm{tran}} = 0$. Two numerical curves marked by the solid circles separate the stability regions of the switching and breathing stationary cyclops states. The black dotted line Γ corresponds to $H'(0) = 0$. Values above the curve make the coupling attractive and full synchronization locally stable. Stationary cyclops states are found as a solution of system (6) and used as initial conditions. The round, diamond, and circled times correspond to the parameters used in Figs. 4–6. (b) The real part of the eigenvalues, associated with the stationary cyclops state, that determine the (internal) stability of the intercluster phase differences (blue solid line) and transversal (external) stability of the first (red dashed line) and second cluster (green dash-dotted line) for fixed $\varepsilon_2 = \varepsilon_2^*$ and varying α_2 [along the white dashed horizontal line in panel (a)]. The background color indicates the type of the emerged cyclops states as in panel (a). (c) The diagram is similar to panel (b), but for fixed $\alpha_2 = \alpha_2^*$ and varying ε_2 [along the black-white dashed vertical line panel (a)]. The shaded area indicates the bistability of switching and breathing cyclops states. Parameters: $N = 11$, $\varepsilon_1 = 1.0$, $\alpha_1 = 1.7$, $\varepsilon_2^* = 0.08$, $\alpha_2^* = 0.78$.

V. STABILITY OF SYNCHRONOUS CLUSTERS

We aim to derive the conditions for transversal stability of the stationary cyclops state (3) that amounts to the stability of the two synchronous clusters composing the stationary cyclops state. We introduce small deviations from the oscillators' phases $\theta_n \longrightarrow \theta_n + \delta\theta_n$, composing the first cluster for $n = 1, \ldots, M-1$ and the second cluster for $n = M+1, \ldots, N$. To study the local stability of each synchronous cluster, we consider the difference variables

$$\xi_n = \delta\theta_{n+1} - \delta\theta_n, \quad n = 1, \ldots, M-2, \tag{16}$$

$$\zeta_n = \delta\theta_{n+1} - \delta\theta_n, \quad n = M+1, \ldots, N-1 \tag{17}$$

that describe the phase difference dynamics within the first and second clusters, respectively. Therefore, from (1), (3), and (16), (17), we obtain two uncoupled variational equations with time-invariant coefficients. Each of the equations determines the local stability of the corresponding cluster within the cyclops state (3):

$$\mu\ddot{\xi}_n + \dot{\xi}_n + \frac{1}{N}\sum_{q=1}^{2}\varepsilon_q q\Big\{\cos(q\gamma_1 + \alpha_q) + \frac{N-1}{2}[\cos\alpha_q + \cos(q\sigma + \alpha_q)]\Big\}\xi_n = 0, \tag{18}$$

where $n = 1, 2, \ldots, M-2$, and

$$\mu\ddot{\zeta}_n + \dot{\zeta}_n + \frac{1}{N}\sum_{q=1}^{2}\varepsilon_q q\Big\{\cos(q\gamma_2 + \alpha_q) + \frac{N-1}{2}[\cos\alpha_q + \cos(q\sigma - \alpha_q)]\Big\}\zeta_n = 0, \tag{19}$$

where $n = M+1, \ldots, N-1$. The variational equations (18) and (19) are stable iff the time-invariant coefficients of the terms ξ_n and ζ_n are positive. Therefore, we can formulate the stability conditions in the following assertion.

Statement 2. [Transversal stability of stationary cyclops states]. Clusters of oscillators composing the stationary cyclops state (3) are locally stable iff:

$$\begin{aligned}
&\sum_{q=1}^{2}\varepsilon_q q\cos(q\gamma_1 + \alpha_q) + \frac{N-1}{2}\Big(\sum_{q=1}^{2}\varepsilon_q q\cos\alpha_q + \sum_{q=1}^{2}\varepsilon_q q\cos(q\sigma + \alpha_q)\Big) > 0,\\
&\sum_{q=1}^{2}\varepsilon_q q\cos(q\gamma_2 + \alpha_q) + \frac{N-1}{2}\Big(\sum_{q=1}^{2}\varepsilon_q q\cos\alpha_q + \sum_{q=1}^{2}\varepsilon_q q\cos(q\sigma - \alpha_q)\Big) > 0,
\end{aligned} \tag{20}$$

where the left-hand sides of the inequalities (20) are the coefficients of the variational equations (18) and (19).

It is also straightforward to show that the stationary cyclops state is always stable to the shift of all phases by a constant value $\delta\theta_k = \delta\theta$ $(k = 1, \ldots, N)$.

It is worth noticing that the eigenvalues $\lambda_{1,2}^{\mathrm{tran}}$ associated with the variational equations (18) and (19) have multiplicity $M-2$. Thus, the eigenvalues $\lambda_1^{\mathrm{tran}}$ and $\lambda_2^{\mathrm{tran}}$ define the transversal stability of the first $(n = 1, 2, \ldots, M-2)$ and second $(n = M+1, \ldots, N)$ clusters, respectively. Figure 3(a) displays their stability boundaries defined by the

conditions (20) with the left-hand sides set to 0 to correspond to $\mathrm{Re}\lambda_1^{\mathrm{tran}} = 0$ (the red dashed line) and $\mathrm{Re}\lambda_2^{\mathrm{tran}} = 0$ (the green dash-dotted line). To highlight the constructive role of the second-harmonic coupling with $\varepsilon_2 \neq 0$, we chose the parameter values that yield unstable stationary cyclops in the network with only first-harmonic coupling with $\varepsilon_2 = 0$ (see Fig. 3).

As Fig. 3(a) indicates, crossing the stability boundary (15) (the lower border of the region CS) induces breathing cyclops states in the region BCS (green) in accordance with Statement 1. In turn, crossing the upper border of the region CS, composed of the transveral stability boundaries $\mathrm{Re}\lambda_1^{\mathrm{tran}} = 0$ (the red dashed line) and $\mathrm{Re}\lambda_2^{\mathrm{tran}} = 0$ (the green dash-dotted line) can yield either switching cyclops states in the region SCS (yellow) or asymmetrical, two-cluster states with five- and six-oscillator synchronous clusters (white region 5:6). In the following, we will primarily focus on the properties of emerging breathing and switching cyclops states.

VI. EMERGING BREATHING AND SWITCHING CYCLOPS STATES

We performed numerical calculations using a widely adopted fifth-order Runge-Kutta scheme with a fixed time step 0.01 to further validate our analytical results and predictions. Figure 3 confirmed the two main bifurcation scenarios for destroying the stationary cyclops states and generating breathing and switching cyclops states described by Statements 1 and 2. In the first scenario, complex conjugate eigenvalues $\lambda_{1,2}$, that determine the stability of constant intercluster phase differences x and y via (10), become purely imaginary and induce oscillating $x(t)$ and $y(t)$ [Fig. 4(c)]. As a result, the stationary cyclops state becomes internally unstable; however, the stability of the clusters preserves and guarantees the emergence of a breathing cyclops state [see Figs. 4(a) and 4(d) and Supplemental Movie 1 [68] for the animation of the breathing cyclops state dynamics]. Periodic oscillations of the first two order parameters r_1 and r_2 depicted in Fig. 4(b) are a signature of such a breathing cyclops state. As the distance from the stability boundary of the *CS* region [solid blue line in Fig. 3 a(a)] increases when changing the second-harmonic coupling strength ε_2 and phase lag α_2, the amplitudes of intercluster difference oscillations $x(t)$, $y(t)$, and order parameters $r_1(t)$, $r_2(t)$ increase. It is worth noticing that for the parameters α_1 and ε_1 used in Fig. 3(a), the breathing cyclops state is also stable in the absence of the second-harmonic coupling ($\varepsilon_2 = 0$).

In the second bifurcation scenario determined via Statement 2, the stationary cyclops state loses its transversal stability when one of the eigenvalues $\lambda_{1,2}^{\mathrm{tran}}$ becomes positive [Fig. 5(c)]. Note that the real parts of the other eigenvalues controlling the internal stability of the intercluster differences remain negative, thereby preserving the stable component of the saddle dynamics. While the transversal instability of the cyclops state may lead to its complete destruction, it induces a switching cyclops state [Figs. 5(a) and 5(d)] when the transversal instability is weak [note the slightly positive eigenvalue, depicted by the red nabla in Fig. 5(c)]. This nonstationary cyclops state represents a two-stage repetitive process. During the first relatively long stage, the

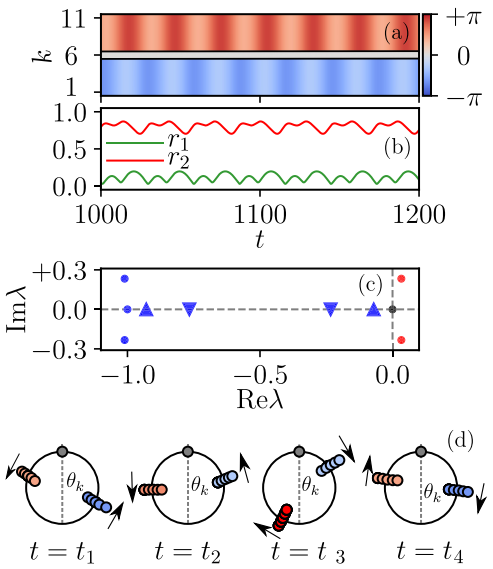

FIG. 4. Breathing cyclops state. (a) The colors depict the phase differences $\theta_k(t) - \theta_6(t)$. The gray strip indicates the reference solitary oscillator. (b) The corresponding values of r_1 and r_2. (c) The eigenvalues associated with the destabilized stationary cyclops state. Some eigenvalues are repeated. The round (triangular) labels correspond to the internal (transversal) stability. Note a pair of complex eigenvalues with a positive real part (red) that emerged due to an Andronov-Hopf bifurcation and yielded periodic oscillations of intercluster differences. (d) Phase distributions θ_k at several time instants. The arrows indicate the direction of periodic phase clusters' oscillations (see Supplemental Movie 1 [68] demonstrating this breathing cyclops state). The oscillators' coloring represents their relative phase difference with the solitary oscillator as in Fig. 2(c). Parameters $N = 11$, $\mu = 1.0$, $\varepsilon_1 = 1.0$, $\alpha_1 = 1.7$, $\varepsilon_2 = 0.08$, $\alpha_2 = -0.1$ correspond to the open circle label in Fig. 3(a).

intercluster differences x and y practically do not change, and the synchronous clusters preserve their formation, i.e., the dynamical pattern is similar to a stationary cyclops state (Fig. 5). During the second short stage, one cluster reshuffles so that one node leaves the unstable cluster to become a new solitary oscillator, whereas the remaining oscillators from the cluster merge with the old solitary node. Figure 5(d) and Supplemental Movie 2 [68] illustrate this process. Accordingly, during the first stage, the magnitudes of the order parameters r_1 and r_2 are practically constant. They undergo an abrupt change during the second stage to return to a constant value [Fig. 5(b)]. As the parameter α_2 increases, the duration of the first stage decreases, and, hence, the period of oscillations in r_1 and r_2 gradually decreases, causing the switching cyclops state to eventually turn into a chaotically switching dynamical pattern (not shown in Fig. 5).

We also observe a hybrid of the switching and breathing cyclops states [Fig. 6(b)]. This hybrid state emerges when, in addition to the external instability of one cluster, there is an internal instability of the intercluster phase differences x and y (Fig. 3). In terms of the eigenvalue spectrum, this amounts to the presence of a pair of complex conjugate eigenvalues $\lambda_{1,2}$ (corresponding to the internal instability) and one real eigenvalue $\lambda_1^{\mathrm{tran}}$ lying to the right from the

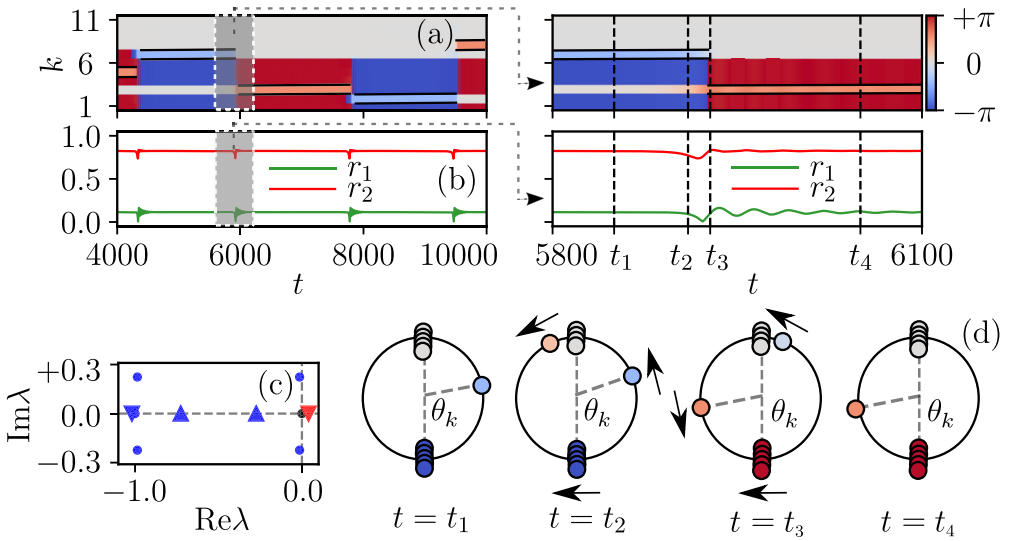

FIG. 5. Switching cyclops state. (a) The colors depict the phase differences $\theta_k(t) - \theta_6(t)$. The strips with solid black borders indicate the reference solitary oscillator during the lifetime of a cyclops state configuration (the first stage). Note that clusters disintegrate to form a new cyclops state with a different solitary oscillator (the second stage). (b) The corresponding values of r_1 and r_2. The gray fragments correspond to the zoomed-in insets (right panels). (c) The eigenvalues associated with the destabilized stationary cyclops state. Some eigenvalues are repeated. The round (triangular) labels correspond to the internal (transversal) stability. Note a positive real eigenvalue (red) corresponding to the loss of the transversal stability of the stationary cyclops state due to Statement 2. (d) Phase distributions θ_k corresponding to a death-birth process in which a cyclops state existing at $t = t_1$ disintegrates to form a new cyclops state at $t = t_4$ (see Supplemental Movie 2 [68] for the details of this dynamical evolution). Parameters $N = 11$, $\mu = 1.0$, $\varepsilon_1 = 1.0$, $\alpha_1 = 1.7$, $\varepsilon_2 = 0.08$, $\alpha_2 = 0.78$ correspond to the diamond label in Fig. 3(a).

imaginary axis [Fig. 6(c)]. We term this hybrid a *switching-breathing cyclops state*, which is effectively a switching cyclops state, which, during its first stage, has oscillating inter-cluster phase differences $x(t)$ and $y(t)$. Accordingly, the order parameter amplitudes r_1 and r_2 are time-periodic functions [Fig. 6(b)]. Figure 6(d) and Supplemental Movie 3 [68] detail the dynamical evolution of the switching-breathing cyclops state.

Breathing and switching cyclops states can also merge to form another hybrid cyclops state, termed *rotobreathing cyclops states* (Fig. 7) in the range of the second-harmonic phase shift with $|\alpha_2| > \pi/2$ (Fig. 8, the pink regions). Rotobreathing

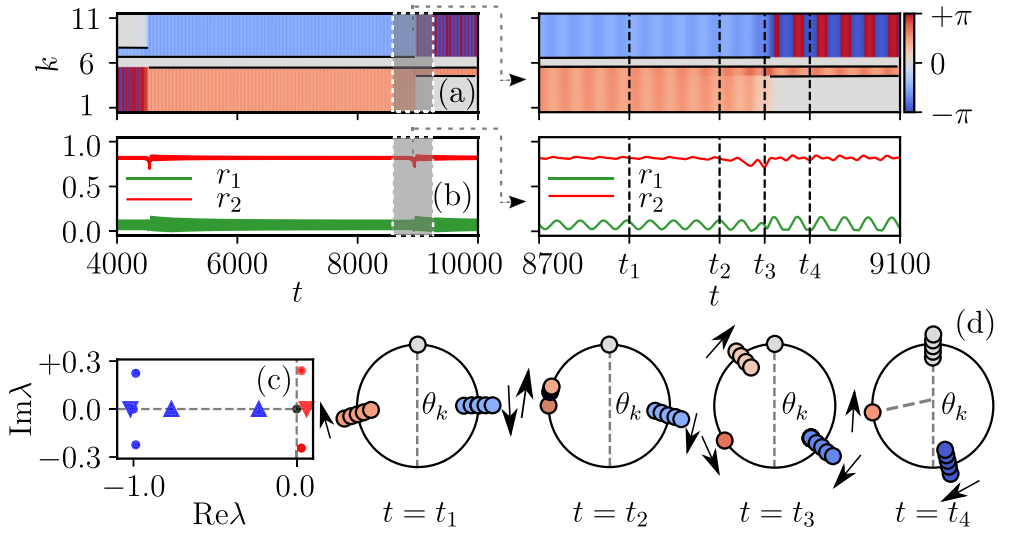

FIG. 6. Switching-breathing cyclops state. The notations are as in Fig. 5. One cluster of the breathing cyclops state [depicted in orange in panel (a)] eventually disintegrates, forming a reshuffled synchronous cluster and a new solitary oscillator. Note the weak internal and transversal instability of the destabilized stationary cyclops state due to the three eigenvalues with small positive real parts [red circles and nabla in panel (c)]. Supplemental Movie 3 [68] animates the sequence given in panel (d). Parameters $N = 11$, $\mu = 1.0$, $\varepsilon_1 = 1.0$, $\alpha_1 = 1.7$, $\varepsilon_2 = 0.0578$, $\alpha_2 = 0.78$ correspond to the circled times label in Fig. 3(a).

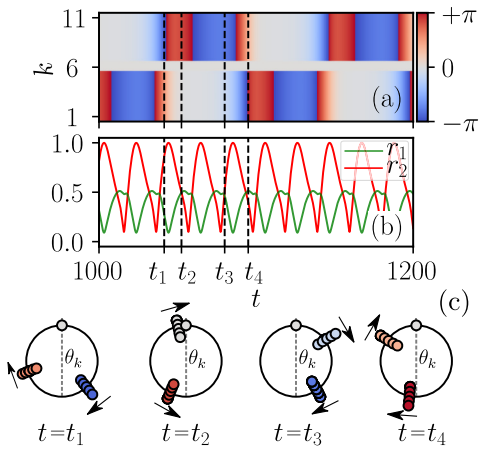

FIG. 7. Rotobreathing cyclops state. The notations are as in Fig. 5. From left to right: the relative phase between the first synchronous cluster and the sixth reference oscillator oscillates, whereas the phase of the second synchronous cluster passes zero and rotates until the clusters exchange their roles. Supplemental Movie 4 [68] details this process. Parameters are $N = 11$, $\mu = 1.0$, $\varepsilon_1 = 1.0$, $\alpha_1 = 1.7$, $\varepsilon_2 = 0.08$, $\alpha_2 = -2.0$.

cyclops states, or simply rotobreathers, are also characterized by a two-stage repetitive process in which, during the first stage, an intercluster phase difference between one cluster and the solitary oscillator oscillates while the relative phase difference of the other cluster rotates. The clusters exchange their oscillatory and rotatory phase roles during the second stage. Figure 7 and Supplemental Movie 4 [68] give the full details of this two-stage process. Accordingly, the amplitudes of the order parameters r_1 and r_2 exhibit large periodic oscillations [Fig. 7(b)].

Figure 8 demonstrates the prevalence of cyclops states of various types. Remarkably, rotobreathers and breathing cyclops states, induced by nonzero second-harmonic phase lag α_2 in the region where full synchronization is unstable, act as global attractors and emerge with a probability close to 1 [Figs. 8(b) and 8(c)]. Note that breathing and switching cyclops states can also emerge with a relatively high probability even when they coexist with presumably dominant full synchronization when the overall coupling is attractive with $H'(0) > 0$ [the region bounded by the black dashed vertical lines in Fig. 8(b); these lines correspond to the solid circles on the black dashed parabola in Fig. 8(a)].

It is worth noting that the globally coupled network (1) with the first- and second-harmonic coupling admits any cluster partition. As a result, stationary cyclops states with a solitary oscillator and nonequally sized coherent clusters exist for even N. However, our extensive simulations suggest that such stationary cyclops states are unstable for even N in the entire parameter range of ε_2 and α_2 considered in this paper. Figure 9(a) supports this claim and demonstrates that, in the attractive coupling case, two-cluster states, coexisting with complete synchronization, are the only stable cluster patterns in the network with $N = 10$. The same claim holds for the repulsive coupling case, with the exception that complete synchronization is no longer stable so that the two-cluster states

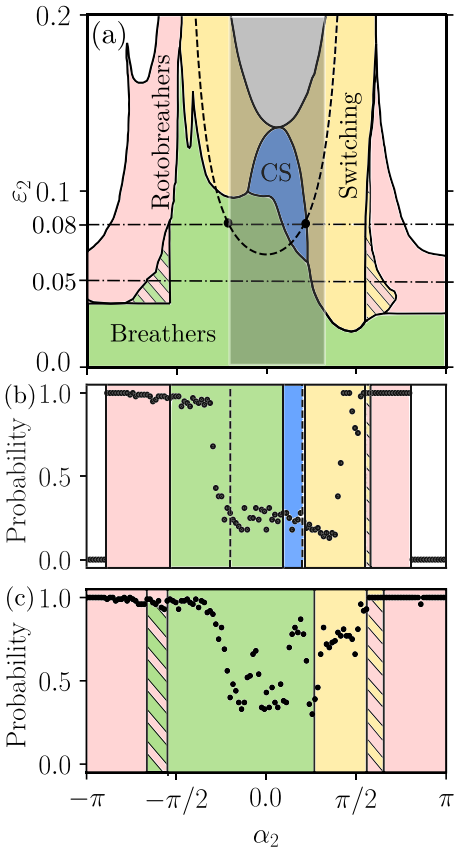

FIG. 8. Stability and prevalence of cyclops states. (a) Stability diagram extending Fig. 3(a) to the full range of the phase lag parameter α_2. The notations are similar to Fig. 3(a), with the addition of rotobreathers (pink). The shaded vertical strip corresponds to the parameter region of Fig. 3(a). Stationary cyclops states in the region *CS* are chosen as initial conditions and further continued by changing the parameter α_2 right and left from each point on the line $\alpha_2 = 0.0$ for each value of ε_2. The initial conditions for the subsequent calculation are carried over from the final state of the preceding computation. The double-shaded areas (inclined stripes) indicate overlapping stability regions and correspond to the bistability of different cyclops state types. The two dash-dotted horizontal lines indicate the values of ε_2 used in panels (b) and (c). (b, c) Probability of cyclops states' emergence (all types). The number of trials is 1000. The initial phases are uniformly distributed in the segment $[-\pi, \pi]$, and the initial velocities are uniformly distributed in the segment $[-1.0, 1.0]$. The black dashed vertical lines in panel (b) indicate the stability boundary of full synchronization. In panel (c) full synchronization is unstable. Parameters are $N = 11$, $\mu = 1.0$, $\varepsilon_1 = 1.0$, $\alpha_1 = 1.7$. (b) $\varepsilon_2 = 0.08$, (c) $\varepsilon_2 = 0.05$.

become prevalent and coexist with four-cluster states with rotating intercluster differences for $N = 10$ [Fig. 9(c)]. Similarly, stationary cyclops states (4) emerge as the only stable patterns along with complete synchronization for $N = 11$ in the attractive coupling case [Fig. 9(b)], and breathing cyclops states with equally sized coherent clusters appear as global attractors in the repulsive coupling case [Fig. 9(d)].

Remarkably, this distinct behavior in the emergence of two-cluster and cyclops states in networks of even and odd sizes carries over to large networks. Figure 10(a) demonstrates

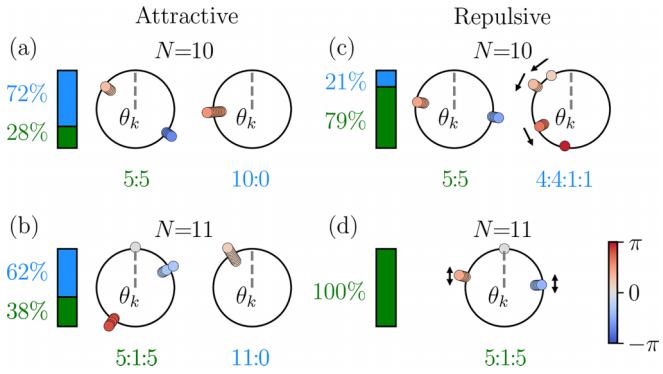

FIG. 9. The probability of occurrence of two-cluster ($N = 10$) and cyclops states ($N = 11$) under attractive and repulsive interactions. The histograms indicate the percentage occurrence of dynamical states in 1000 simulations with random initial conditions. The initial phases $\Theta_k(0)$ are uniformly distributed on $[-\pi, \pi]$; the initial velocities $\dot{\Theta}_k(0)$ are uniformly distributed on $[-5.0, 5.0]$. The snapshots correspond to the established dynamical states with the relative phases θ_k in the rotating frame as in (4). (a, b) Attractive coupling: complete synchronization is prevalent with a 72 % ($N = 10$) and 62 % ($N = 11$) probability. It coexists for $N = 10$ with a stationary two-cluster 5:5 state with an even partition of five oscillators in each cluster and a constant intercluster phase difference (a) and for $N = 11$ with a stationary cyclops state 5:1:5 (b). (c, d) Repulsive coupling. (c) $N = 10$: stationary two-cluster 5:5 states coexist with four-cluster states 4:4:1:1 with nonstationary intercluster phase differences. (d) $N = 11$: breathing cyclops states 5:1:5 with oscillating intercluster phase differences are global attractors emerging with a 100% probability. The black arrows indicate the directions of evolving intercluster differences. Parameters are $\mu = 1.0$, $\varepsilon_1 = 1.0$, $\alpha_1 = 1.7$; (a, b) $\varepsilon_2 = 0.12$, $\alpha_2 = 0.0$; (c, d) $\varepsilon_2 = 0.04$, $\alpha_2 = 0.6$.

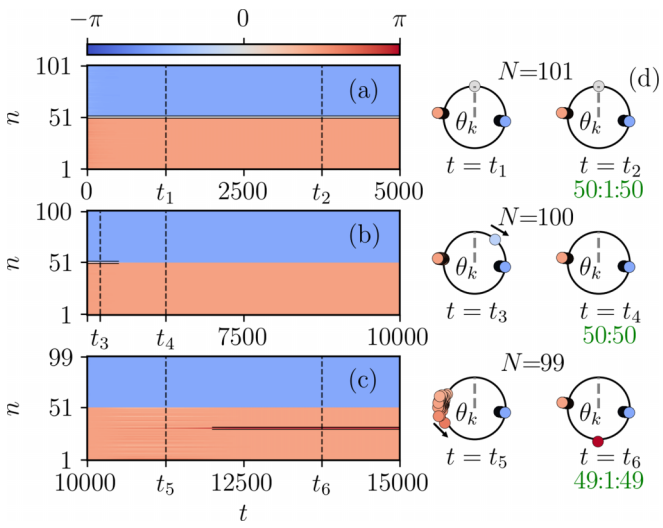

FIG. 10. Odd vs even-sized large networks: the transition between cyclops and two-cluster states as N changes. The colors depict the relative phases θ_k, $k = 1, \ldots, N$. (a) A cyclops state with the three-cluster partition 50:1:50 in the 101-oscillator network. The cyclops state with small phase offsets, randomly chosen from a uniform distribution $[-0.01; 0.01]$ was selected as the initial condition. The horizontal black stripe indicates the solitary oscillator with $\theta_{51} = 0$. (b) The emergence of a two-cluster state 50:50 in the 100-oscillator network. The cyclops state from (a) with one oscillator removed from the second cluster was selected as the initial condition. (c) Removing one oscillator from the two-cluster state in (b) induces a cyclops state 49:1:49 in the 99-oscillator network. (d) The corresponding snapshots of phases θ_k at several time instants: $t_1 = 1250$, $t_2 = 3750$, $t_3 = 5200$, $t_4 = 6250$, $t_5 = 11\,250$, and $t_6 = 13\,750$. The black arrow indicates the direction of the solitary oscillator's phase evolution. Parameters are $\mu = 1.0$, $\varepsilon_1 = 1.0$, $\alpha_1 = 3.1$, $\varepsilon_2 = 0.002$, $\alpha_2 = 0.2$.

that stationary cyclops states (4) are stable in the odd-sized network with $N = 101$. Eliminating one oscillator from the network turns the cyclops state into a two-cluster state with equally sized clusters [Fig. 10(b)]. Removing an extra oscillator from this 100-node network transforms the two-cluster state back to a stationary cyclops state [Fig. 10(c)]. We expect this effect to persist in the thermodynamic limit of very large N.

VII. PERSISTENCE OF CYCLOPS STATES

In this section we demonstrate that cyclops states resist intrinsic frequency detuning. We mismatch the intrinsic frequency ω by choosing the kth oscillator's frequency ω_k, $k = 1, \ldots N$ from a uniform random distribution in the interval $[\omega - \delta, \omega + \delta]$, where δ is a frequency detuning. We consider the parameter region where stationary cyclops states are stable [region *CS* in Fig. 3(a)]. Figure 11 demonstrates the persistence of three stationary cyclops states, each induced by a particular intrinsic frequency distribution. Note that although the oscillators' phases within each synchronous cluster may not perfectly align due to the frequency detuning, they remain relatively close to each other (see Fig. 11). Additionally, the established frequencies of all oscillators are the same. The stationary cyclops state can lose the transversal stability similarly to their counterparts from the identical oscillator case (note the stationary cyclops state marked by the red labels in Fig. 11 that turns into a switching cyclops state at $\delta = \delta_1$). Remarkably, the frequency detuning can also induce a bifurcation scenario for disintegrating stationary cyclops states via a saddle-node bifurcation at $\delta = \delta_2$ and $\delta = \delta_3$. We did not observe such a bifurcation route in our extensive simulations of system (1) with identical frequencies reported in Figs. 3–8.

VIII. CONCLUSIONS

Building upon our recent study [50], this work has significantly advanced an understanding of rhythmogenesis in Kuramoto networks of 2D phase oscillators with first-mode and higher-mode coupling. A key focus of our work has been on the constructive role of higher coupling modes in inducing and stabilizing a unique class of dynamical states known as cyclops states. These states, characterized by two coherent clusters and a solitary oscillator resembling the Cyclops's eye, represent a particular form of three-cluster generalized splay states [49].

Our initial findings in [50] revealed the unexpected result that adding the second or third harmonic to the Kuramoto coupling makes cyclops states global attractors, exhibiting remarkable stability over a substantial range of coupling's repulsion. This paper delved deeper into the dynamic repertoire of cyclops states, introducing and systematically analyzing

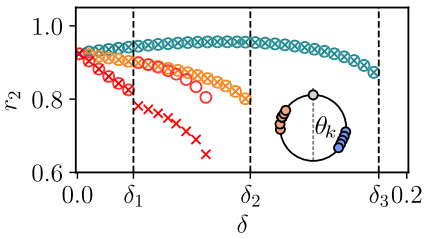

FIG. 11. Persistence of cyclops states in system (1) with mismatched frequencies ω_k distributed evenly over the interval $[\omega - \delta,\ \omega + \delta]$, where $\omega = 1.7$ and δ is a frequency detuning. Global maxima (circles) and minima (crosses) of order parameter r_2 for three cyclops states (red, orange, and cyan). The global maximum was determined in the time interval $5 \times 10^3 \leqslant t \leqslant 10^4$ following the transition process. A stationary cyclops state is indicated by overlapping circles and crosses of the same color, while separated circles and crosses denote a switching cyclops state. The first cyclops state (red) originates from the original intrinsic frequency distribution. Subsequently, modifying the distribution by exchanging the intrinsic frequency of the Mth solitary oscillator, ω_M, with ω_1 (or ω_{M+1}) induces the emergence of the second (or third) cyclops state, depicted by orange and cyan, respectively. As the parameter mismatch δ increases, the distribution of mismatched frequencies widens. To induce each of the three cyclops states as δ increases, a stationary cyclops state from the identical frequency case was used as the initial condition for $\delta = 0$. The final phase distribution at a given δ is then used as initial conditions for subsequent simulations at a higher value of δ. The values of $\delta < \delta_1$ preserve all three stable stationary cyclops states. Increasing $\delta > \delta_1$ destabilizes the first stationary cyclops state (red) and turns it into a switching cyclops state. Further increasing $\delta > \delta_2$ leads to disintegrating the second cyclops state (orange) at $\delta = \delta_2$. The third stationary cyclops state (cyan) persists to $\delta = \delta_3$. The cyclops states are found from direct numerical simulations of system (1) for three sets of natural frequency distributions ω_k with a continuous increase in δ from zero. The inset shows instantaneous phase distributions θ_k for the third cyclops state with nonidentical frequencies. Parameters are $N = 11$, $\mu = 1.0$, $\varepsilon_1 = 1.0$, $\alpha_1 = 1.8$, $\varepsilon_2 = 0.12$. The bifurcation parameter values are $\alpha_2 = 0.2$, $\delta_1 = 0.034$, $\delta_2 = 0.105$, $\delta_3 = 0.183$.

breathing and switching cyclops states and their hybrids, including switching-breathing cyclops states and rotobreathers. Through rigorous analytical derivations and numerics, we have identified conditions for the existence and stability of stationary cyclops states, elucidating two distinct bifurcation scenarios. In both scenarios, the second coupling harmonic acts as a constructive agent, either inducing periodic oscillations in intercluster relative phase differences (breathing cyclops states) or facilitating swift reconfigurations and transitions (switching cyclops states). These dynamical patterns can be viewed as nontrivial hybrids of solitary states [41–44], generalized splay [49], clusters with breathing and rotatory intercluster phase shifts [46,47], and intermittent [37] and switching chimeras [64]. In particular, switching cyclops states unite the properties of blinking chimeras [64] and three-cluster states [47].

Our extensive stability analysis has underscored the resilience and dominance of breathing, rotobreathing, and switching cyclops states across wide parameter ranges, including the case of the overall attractive, two-harmonic coupling. Importantly, we have showcased that the constructive influence of higher coupling harmonics is not limited to networks of identical oscillators, as cyclops states persist robustly in Kuramoto networks of nonidentical oscillators.

Importantly, our prior work [50] demonstrated the dynamic equivalence of the 2D Kuramoto model with first- and second-harmonic coupling to a network of canonical theta neurons with adaptive coupling. This equivalence also suggests the widespread manifestation of breathing and switching cyclops states in theta-neuron networks, underscoring our results' broad applicability and significance in diverse physical and biological networks.

While it is crucial to differentiate between the higher-order harmonic coupling studied in this paper and the higher-order nonpairwise coupling [69–72], it is equally important to recognize their possible interplay and the richness they bring to the dynamics of networked systems. These concepts are not mutually exclusive; they can coexist, adding layers of complexity and fostering a diverse range of emergent behaviors. Recent research [73,74] analyzed the intricate interplay between pairwise first-order harmonic and nonpairwise higher-order coupling in shaping collective dynamics in Kuramoto networks. The incorporation of both higher-order harmonics and nonpairwise interactions promises to induce even richer emerging dynamics, including various forms of cyclops states, and may pave the way for a more holistic comprehension of complex networked systems.

ACKNOWLEDGMENTS

This work was supported by the Ministry of Science and Higher Education of the Russian Federation under project No. 0729-2020-0036 (to G. V. O. and M. I. B.), the Russian Science Foundation under project No. 22-12-00348 (to V. O. M. and L. A. S.), the National Science Foundation (USA) under Grant No. CMMI-2009329, and the Office of Naval Research under Grant No. N00014-22-1-2200 (to I. B.)

APPENDIX: MAXIMUM NUMBER OF STATIONARY CYCLOPS STATES

Here, we provide the details for deriving an upper bound for the maximum number of stationary cyclops states with distinct x and y, given in Sec. III.

Finding all possible solutions of system (6) that determine the existence of stationary cyclops states is elusive due to its complexity, and the number of solutions can vary depending on the parameters. In particular, it prevents locating all solutions of the system (6) by their continuation with respect to the parameters. However, this computational problem can be simplified by the change of variables $u = e^{ix}$, $v = e^{iy}$ ($|u| = 1$, $|v| = 1$) that transforms the real-valued system (6) into the system of complex polynomial equations:

$$(1-u)\left\{uv\left[e^{i\alpha_1}\left(u+v+\frac{2uv}{N-1}\right)\right.\right.$$
$$\left.\left.+e^{-i\alpha_1}v\left(u+v+\frac{2}{N-1}\right)\right]\right.$$

$$
\begin{aligned}
&+\varepsilon_2(u+1)\left[e^{i\alpha_2}\left(u^2+v^2+\frac{2u^2v^2}{N-1}\right)\right.\\
&\left.\left.+e^{-i\alpha_2}v^2\left(u^2+v^2+\frac{2}{N-1}\right)\right]\right\}=0,\\
(1-v)&\left\{uv\left[e^{i\alpha_1}\left(u+v+\frac{2uv}{N-1}\right)\right.\right.\\
&\left.+e^{-i\alpha_1}u\left(u+v+\frac{2}{N-1}\right)\right]\\
&+\varepsilon_2(v+1)\left[e^{i\alpha_2}\left(u^2+v^2+\frac{2u^2v^2}{N-1}\right)\right.\\
&\left.\left.+e^{-i\alpha_2}u^2\left(u^2+v^2+\frac{2}{N-1}\right)\right]\right\}=0. \qquad \text{(A1)}
\end{aligned}
$$

The analysis of system (A1) is more manageable, and the maximum number of its solutions (the roots of the complex polynomials) can be estimated by applying the classical Bernshtein theorem from algebra. To facilitate the reading, we list this theorem below.

Theorem [Bernshtein, 1975] [67]. Let a system of n polynomials have a finite number of roots in $(C^*)^n$, where $C^* = C \setminus 0$. Then, the number of roots is bounded from above by the mixed volume P_k of their Newton polytopes (the convex hull of polynomial supports S_k).

Before applying the theorem to (A1), we get rid of the factors $(1-u)$ and $(1-v)$ on the right-hand side of (A1) since we are interested only in solutions $u, v \neq 1$. By doing so, we have excluded the solutions that correspond to a one-cluster solution and two-cluster solutions of the form $(N-1)/2{:}(N+1)/2$. It is worth mentioning that, in contrast to its real-valued counterpart (6), the complex polynomials may have either nonphysical solutions with $|u| \neq 1$ or $|v| \neq 1$, or solutions that do not correspond to stationary cyclops states. The latter solutions with $|u| = 1$ and $|v| = 1$, include a two-cluster $N-1:1$ solitary state, corresponding to $u = v$, i.e., $x = y$.

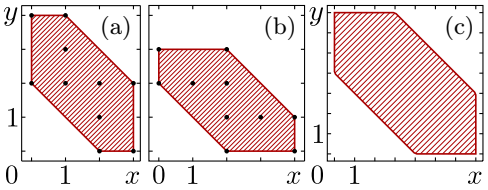

FIG. 12. The supports S_1, S_2 (black dots) and the corresponding Newton polytopes P_1, P_2 (shaded regions) of (a) the first and (b) second polynomials of system (A1). (c) The Minkowski sum $P_1 \oplus P_2$.

The support of a polynomial $\sum_j \sum_l a_{jl} u^j v^l$ is the set of exponents (j, l). Thus, the supports S_1 and S_2 of the resulting polynomials (degrees u and v in each of the first and second equations terms) have the form $S_1 = \{(0,2);(0,4);(1,2);(1,3);(1,4);(2,0);(2,1);(2,2);(3,0);(3,2)\}$, $S_2 = \{(0,2);(0,3);(1,2);(2,0);(2,1);(2,2);(2,3);(3,1);(4,0);(4,1)\}$.

Consider the mixed volume of Newtonian polytopes P_1 and P_2: $M(P_1, P_2) = \mathrm{vol}_2(P_1 \oplus P_2) - \mathrm{vol}_2(P_1) - \mathrm{vol}_2(P_2)$. As we need to handle only two equations, determining the mixed volume of the two Newtonian polytopes is straightforward and amounts to computing the area of the shaded regions in Fig. 12. This yields the following values: $\mathrm{vol}_2(P_1) = 8$, $\mathrm{vol}_2(P_2) = 8$, $\mathrm{vol}_2(P_1 \oplus P_2) = 33$ (see Fig. 12). Therefore, $M(P_1, P_2) = 17$. Excluding the nonphysical solutions and solutions corresponding to noncyclops regimes from the sets of roots in (A1), we can always find the number of cyclops modes in the system (1), which is limited to 16 cyclops states.

Our numerical search for the roots of polynomials (A1) was performed using the NSolve function of Wolfram *Mathematica*. This search found 17 roots almost everywhere in the considered broad parameter regions, suggesting that our analysis effectively identified all possible solutions of (A1) and, therefore, all possible stationary states cyclops, identified from the 17 solutions by excluding the nonphysical solutions ($|u| \neq 1$ or $|v| \neq 1$) and noncyclops states ($u = 1$ or $v = 1$ or $u = v$).

[1] J. Rinzel and G. B. Ermentrout, Methods Neuronal Model. **2**, 251 (1998).
[2] G. B. Ermentrout and D. Kleinfeld, Neuron **29**, 33 (2001).
[3] F. C. Hoppensteadt and E. M. Izhikevich, *Weakly Connected Neural Networks*, Applied Mathematical Sciences (Springer, New York, NY, 2012), Vol. 126.
[4] G. Kozyreff, A. G. Vladimirov, and P. Mandel, Phys. Rev. Lett. **85**, 3809 (2000).
[5] J. Ding, I. Belykh, A. Marandi, and M.-A. Miri, Phys. Rev. Appl. **12**, 054039 (2019).
[6] N. Nair, K. Hu, M. Berrill, K. Wiesenfeld, and Y. Braiman, Phys. Rev. Lett. **127**, 173901 (2021).
[7] A. E. Motter, S. A. Myers, M. Anghel, and T. Nishikawa, Nat. Phys. **9**, 191 (2013).
[8] F. Dörfler, M. Chertkov, and F. Bullo, Proc. Natl. Acad. Sci. USA **110**, 2005 (2013).
[9] R. Berner, S. Yanchuk, and E. Schöll, Phys. Rev. E **103**, 042315 (2021).
[10] Y. Kuramoto, in *International Symposium on Mathematical Problems in Theoretical Physics*, edited by H. Araki (Kyoto University, Kyoto, Japan, 1975), pp. 420–422.
[11] S. H. Strogatz, Physica D **143**, 1 (2000).
[12] B. Ermentrout and M. Lewis, Bull. Math. Biol. **59**, 533 (1997).
[13] J. A. Acebrón, L. L. Bonilla, C. J. P. Vicente, F. Ritort, and R. Spigler, Rev. Mod. Phys. **77**, 137 (2005).
[14] E. Barreto, B. Hunt, E. Ott, and P. So, Phys. Rev. E **77**, 036107 (2008).
[15] E. Ott and T. M. Antonsen, Chaos **18**, 037113 (2008).
[16] H. Hong, H. Chaté, H. Park, and L.-H. Tang, Phys. Rev. Lett. **99**, 184101 (2007).
[17] A. Pikovsky and M. Rosenblum, Phys. Rev. Lett. **101**, 264103 (2008).

[18] Y. Maistrenko, O. Popovych, O. Burylko, and P. A. Tass, Phys. Rev. Lett. **93**, 084102 (2004).

[19] F. Dörfler and F. Bullo, SIAM J. Appl. Dyn. Syst. **10**, 1070 (2011).

[20] H.-A. Tanaka, A. J. Lichtenberg, and S. Oishi, Phys. Rev. Lett. **78**, 2104 (1997).

[21] H.-A. Tanaka, A. J. Lichtenberg, and S. Oishi, Physica D **100**, 279 (1997).

[22] P. Ji, T. K. Peron, F. A. Rodrigues, and J. Kurths, Sci. Rep. **4**, 4783 (2014).

[23] V. Munyaev, L. Smirnov, V. Kostin, G. Osipov, and A. Pikovsky, New J. Phys. **22**, 023036 (2020).

[24] M. Komarov, S. Gupta, and A. Pikovsky, EPL (Europhys. Lett.) **106**, 40003 (2014).

[25] E. A. Martens, E. Barreto, S. H. Strogatz, E. Ott, P. So, and T. M. Antonsen, Phys. Rev. E **79**, 026204 (2009).

[26] N. V. Barabash, V. N. Belykh, G. V. Osipov, and I. V. Belykh, Chaos **31**, 113113 (2021).

[27] J. Gómez-Gardenes, S. Gómez, A. Arenas, and Y. Moreno, Phys. Rev. Lett. **106**, 128701 (2011).

[28] P. Ji, T. K. DM. Peron, P. J. Menck, F. A. Rodrigues, and J. Kurths, Phys. Rev. Lett. **110**, 218701 (2013).

[29] P. S. Skardal and A. Arenas, Phys. Rev. E **89**, 062811 (2014).

[30] T. Nishikawa and A. E. Motter, Phys. Rev. Lett. **117**, 114101 (2016).

[31] Z. G. Nicolaou, D. Eroglu, and A. E. Motter, Phys. Rev. X **9**, 011017 (2019).

[32] Y. Kuramoto and D. Battogtokh, Nonlinear Phenom. Complex Syst. **5**, 380 (2002).

[33] D. M. Abrams and S. H. Strogatz, Phys. Rev. Lett. **93**, 174102 (2004).

[34] D. M. Abrams, R. Mirollo, S. H. Strogatz, and D. A. Wiley, Phys. Rev. Lett. **101**, 084103 (2008).

[35] M. J. Panaggio and D. M. Abrams, Nonlinearity **28**, R67 (2015).

[36] A. Zakharova, M. Kapeller, and E. Schöll, Phys. Rev. Lett. **112**, 154101 (2014).

[37] S. Olmi, E. A. Martens, S. Thutupalli, and A. Torcini, Phys. Rev. E **92**, 030901(R) (2015).

[38] M. I. Bolotov, G. V. Osipov, and A. Pikovsky, Phys. Rev. E **93**, 032202 (2016).

[39] M. Bolotov, L. Smirnov, G. Osipov, and A. Pikovsky, Chaos **28**, 045101 (2018).

[40] P. Jaros, Y. Maistrenko, and T. Kapitaniak, Phys. Rev. E **91**, 022907 (2015).

[41] Y. Maistrenko, S. Brezetsky, P. Jaros, R. Levchenko, and T. Kapitaniak, Phys. Rev. E **95**, 010203(R) (2017).

[42] P. Jaros, S. Brezetsky, R. Levchenko, D. Dudkowski, T. Kapitaniak, and Y. Maistrenko, Chaos **28**, 011103 (2018).

[43] E. Teichmann and M. Rosenblum, Chaos **29**, 093124 (2019).

[44] V. O. Munyayev, M. I. Bolotov, L. A. Smirnov, G. V. Osipov, and I. V. Belykh, Phys. Rev. E **105**, 024203 (2022).

[45] S. Olmi, A. Navas, S. Boccaletti, and A. Torcini, Phys. Rev. E **90**, 042905 (2014).

[46] I. V. Belykh, B. N. Brister, and V. N. Belykh, Chaos **26**, 094822 (2016).

[47] B. N. Brister, V. N. Belykh, and I. V. Belykh, Phys. Rev. E **101**, 062206 (2020).

[48] R. Ronge and M. A. Zaks, Eur. Phys. J.: Spec. Top. **230**, 2717 (2021).

[49] R. Berner, S. Yanchuk, Y. Maistrenko, and E. Scholl, Chaos **31**, 073128 (2021).

[50] V. O. Munyayev, M. I. Bolotov, L. A. Smirnov, G. V. Osipov, and I. Belykh, Phys. Rev. Lett. **130**, 107201 (2023).

[51] L. S. Tsimring, N. F. Rulkov, M. L. Larsen, and M. Gabbay, Phys. Rev. Lett. **95**, 014101 (2005).

[52] Y.-C. Gao, C.-J. Fu, S.-M. Cai, C. Yang, and H. Eugene Stanley, Chaos **29**, 053130 (2019).

[53] I. Belykh and A. Shilnikov, Phys. Rev. Lett. **101**, 078102 (2008).

[54] T. Nishikawa and A. E. Motter, Proc. Natl. Acad. Sci. USA **107**, 10342 (2010).

[55] I. Belykh, R. Reimbayev, and K. Zhao, Phys. Rev. E **91**, 062919 (2015).

[56] R. Reimbayev, K. Daley, and I. Belykh, Philos. Trans. R. Soc. A **375**, 20160282 (2017).

[57] P. Seliger, S. C. Young, and L. S. Tsimring, Phys. Rev. E **65**, 041906 (2002).

[58] R. K. Niyogi and L. Q. English, Phys. Rev. E **80**, 066213 (2009).

[59] I. Z. Kiss, Y. Zhai, and J. L. Hudson, Phys. Rev. Lett. **94**, 248301 (2005).

[60] E. Goldobin, R. Kleiner, D. Koelle, and R. G. Mints, Phys. Rev. Lett. **111**, 057004 (2013).

[61] M. Komarov and A. Pikovsky, Phys. Rev. Lett. **111**, 204101 (2013).

[62] R. Berner, A. Lu, and I. M. Sokolov, Chaos **33**, 073138 (2023).

[63] P. S. Skardal, E. Ott, and J. G. Restrepo, Phys. Rev. E **84**, 036208 (2011).

[64] R. J. Goldschmidt, A. Pikovsky, and A. Politi, Chaos **29**, 071101 (2019).

[65] H. Sakaguchi, and Y. Kuramoto, Prog. Theor. Phys. **76**, 576 (1986).

[66] H. Daido, Prog. Theor. Phys. **88**, 1213 (1992).

[67] D. N. Bernshtein, Funktsional'nyi Analiz i Ego Prilozheniya **9**, 1 (1975).

[68] See Supplemental Material at http://link.aps.org/supplemental/10.1103/PhysRevE.109.054202 for supplemental movies for Figs. 4–7.

[69] L. V. Gambuzza, F. Di Patti, L. Gallo, S. Lepri, M. Romance, R. Criado, M. Frasca, V. Latora, and S. Boccaletti, Nat. Commun. **12**, 1255 (2021).

[70] C. Xu and P. S. Skardal, Phys. Rev. Res. **3**, 013013 (2021).

[71] A. P. Millán, J. J. Torres, and G. Bianconi, Phys. Rev. Lett. **124**, 218301 (2020).

[72] S. Boccaletti, P. De Lellis, C. del Genio, K. Alfaro-Bittner, R. Criado, S. Jalan, and M. Romance, Phys. Rep. **1018**, 1 (2023).

[73] A. Carballosa, A. P. Muñuzuri, S. Boccaletti, A. Torcini, and S. Olmi, Chaos Solitons Fractals **177**, 114197 (2023).

[74] P. Jaros, S. Ghosh, D. Dudkowski, S. K. Dana, and T. Kapitaniak, Phys. Rev. E **108**, 024215 (2023).